ACS APPLIED MATERIALS & INTERFACES

Research Article

www.acsami.org

Fabrication of Graphene-Encapsulated Porous Carbon–Metal Oxide Composites as Anode Materials for Lithium-Ion Batteries

Shanshan Tao,[†] Wenbo Yue,*[,†] Meiyan Zhong,[†] Zhaojing Chen,[†] and Yu Ren*[,‡]

[†]Beijing Key Laboratory of Energy Conversion and Storage Materials, College of Chemistry, Beijing Normal University, Beijing 100875, P. R. China

[‡]National Institute of Clean-and-Low-Carbon Energy, Beijing 102209, P. R. China

Supporting Information

ABSTRACT: Porous carbons such as CMK-3 are commonly used as matrices to accommodate metal oxides for the improvement of their electrochemical performance. However, the mesostructure of CMK-3 may be destroyed gradually with the increase of metal oxide content and some particles are inevitably formed outside the pores of CMK-3, leading to a gradual decrease in capacity and poor cycling performance. Herein, graphene-encapsulated CMK-3-metal oxides (Fe_3O_4 and NiO) are synthesized through a stepwise heterocoagulation method and exhibit improved electrochemical performances compared to uncoated CMK-3-metal oxides. The core–shell structure of these novel composites can protect the metal oxide particles on the surface of CMK-3 and avoid the aggregation of porous carbon–metal oxides. Moreover, the introduction of graphene may stabilize the mesostructure of CMK-3 during lithiation and delithiation processes and improve the electronic conductivity of the composite, which are conducive to enhancing electrochemical performances of porous carbon-supported metal oxides.

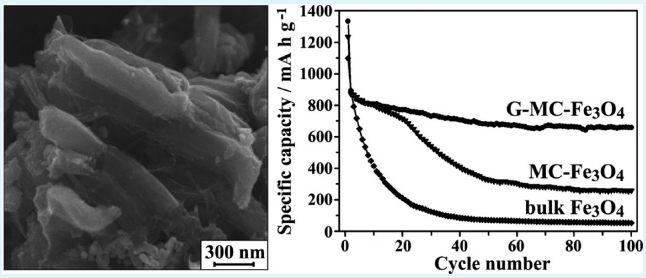

KEYWORDS: *porous carbon, ferroferric oxide, nickel oxide, graphene, lithium-ion battery*

INTRODUCTION

The development of lithium-ion batteries (LIBs) with high energy density and long cycle life is much in demand owing to their extensive applications in portable electronic devices and electric vehicles. As promising high-capacity anodes for LIBs, metal oxides are expected to replace the conventional graphite anode due to their high theoretical capacities, natural abundance, and low cost. The theoretical capacity of the conventional graphite anode is only ~370 mA h g^{-1}, much lower than that of Fe_3O_4 (924 mA h g^{-1}) or NiO (718 mA h g^{-1}).[1,2] However, the volume variation of metal oxides during the charge–discharge process and the poor electronic conductivity of metal oxides may lead to a gradual decrease in capacity and poor cycling performance, hindering their practical use in LIBs.[3,4] Some effective methods have been developed to overcome these problems. For instance, fabrication of nanoscale or hollow metal oxide electrodes may relatively accommodate their volume change during cycles, giving rise to the improvement of the electrochemical performances.[5,6] Alternatively, carbon matrices used to support metal oxides may also enhance the cycle performances and rate capabilities of metal oxide electrodes.[7,8] In particular, porous carbons such as CMK-3 inherit the advantages of normal carbonaceous and porous materials: (i) The pores of CMK-3 can limit the particle size of metal oxides and accommodate the volume variation of metal oxides during cycles. (ii) The mesostructure of CMK-3 can avoid the aggregation of metal oxide particles and protect them against disintegration. (iii) CMK-3 can also improve the electronic conductivity of the composite. Accordingly, CMK-3-supported metal oxides usually exhibit better electrochemical properties than pure metal oxide particles.[9−12]

Generally, two strategies are employed for the preparation of CMK-3-metal oxide composites. One is the one-step method that both metal oxide precursor (e.g., metal nitrate) and carbon precursor (e.g., sucrose) are introduced into the pores of mesoporous silica (e.g., SBA-15) and calcined under N_2 protection. CMK-3-metal oxides are directly formed inside the pores of SBA-15 and obtained after removal of SBA-15 template in NaOH or HF solution.[13] However, the formed metal oxide particles are mainly embedded or lodged in the wall of CMK-3, which cannot provide high lithium storage capacities. The other is the two-step method that CMK-3 is first prepared using SBA-15 as the template, and metal oxide particles are subsequently formed in the pores of CMK-3.[14,15] Owing to the low theoretical capacity of CMK-3, the CMK-3 composite with high loading of metal oxides is desirable and can be achieved by the two-step method. Nevertheless, the mesostructure of CMK-3 may be destroyed gradually with the increase of metal oxide content, and some metal oxide particles

Received: December 2, 2013
Accepted: April 25, 2014
Published: April 25, 2014

   dx.doi.org/10.1021/am501551h | ACS Appl. Mater. Interfaces 2014, 6, 6332–6339

are inevitably formed outside the pores of CMK-3.[16,17] In addition, the pores of CMK-3 may also collapse during Li-ion intercalation and deintercalation processes. Therefore, these composites usually display high reversible capacities in the initial cycles and decreased capacities in the following cycles. It is still a formidable challenge to protect the particles on the surface of CMK-3 and stabilize the framework of carbon matrices during lithiation and delithiation processes.

As a novel carbon nanosheet, graphene possesses many advantages such as outstanding mechanical and electronic properties, and is used as a matrix to support metal oxides.[18] In the last 5 years, graphene-encapsulated or graphene-based metal oxides have been fabricated as high-performance anode materials for LIBs.[19−22] The superior electrochemical behavior of these composites may be ascribed to the graphene support, which improves the electronic conductivity of the composite and restrains the volume variation of metal oxides during cycling.[23,24] Furthermore, our previous work demonstrates that graphene nanosheets may stabilize the mesostructure of porous metal oxides during the charge−discharge process.[19,20] Herein, graphene-encapsulated CMK-3-metal oxides (Fe_3O_4 and NiO) were successfully synthesized by a stepwise heterocoagulation method and exhibited better cycle performances and rate capabilities compared to uncoated CMK-3-metal oxides. This synthesis technique can be further extended to the preparation of other graphene-porous carbon−metal oxide composites with applications in supercapacitors and LIBs.

EXPERIMENTAL SECTION

CMK-3 was synthesized using sucrose as the precursor and SBA-15 as the template (see the Supporting Information).[25] CMK-3-metal oxides were synthesized by thermal decomposition of metal nitrates inside the pores of CMK-3 under N_2 protection. In brief, CMK-3 was first treated in nitric acid by ultrasonication for 0.5 h. Subsequently, 4.0 g of $Fe(NO_3)_3{\cdot}9H_2O$ or 3.2 g of $Ni(NO_3)_2{\cdot}6H_2O$ was dissolved in 20 mL of ethanol and then 0.5 g of CMK-3 was added into this solution. After stirring for 1 h, the ethanol was completely evaporated under vacuum at 70 °C. The dried powder was transferred into the tubular furnace and heated under N_2 protection at 500 °C for 3 h to obtain CMK-3-Fe_3O_4 or at 400 °C for 3 h to obtain CMK-3-NiO.

Graphene oxide (GO) was synthesized using a modified Hummer's method (see the Supporting Information).[26] Graphene-encapsulated CMK-3-metal oxides were synthesized by a stepwise heterocoagulation method.[19,27] In brief, 0.01 g of GO and 0.04 g of CMK-3-Fe_3O_4 (or CMK-3-NiO) were dispersed in 80 mL of H_2O by ultrasonication for 0.5−1 h, respectively. The pH of GO solution was adjusted to ∼8.0 with aqueous ammonia, and the pH of CMK-3-metal oxide suspension was adjusted to ∼5.5 with dilute hydrochloric acid. Then the CMK-3-metal oxide suspension was added into the GO solution under mild magnetic stirring. After 1 h, 0.4 g of L-ascorbic acid was added into the above mixture under N_2 protection with stirring for 24 h. The graphene-encapsulated CMK-3-metal oxides were collected by centrifugation, washed with deionized water, and then dried at 60 °C. The uncoated CMK-3-metal oxides were denoted as MC-Fe_3O_4 and MC-NiO, and the graphene-encapsulated composites were referred to as G-MC-Fe_3O_4 and G-MC-NiO, respectively. Graphene-encapsulated CMK-3 (G-MC) without metal oxides was also prepared by HCl etching of Fe_3O_4 particles.

Detailed characterization and electrochemical test methods could be found in our recent reports (see the Supporting Information).[20,27]

RESULTS AND DISCUSSION

The overall synthesis procedure of CMK-3-Fe_3O_4/NiO (referred to as MC-Fe_3O_4/NiO) and graphene-encapsulated CMK-3-Fe_3O_4/NiO (referred to as G-MC-Fe_3O_4/NiO) is illustrated in Scheme 1. The metal oxide precursors were first

Scheme 1. Schematic Illustration of Synthesis Routes of (a) MC-Metal Oxides and (b) G-MC-Metal Oxides

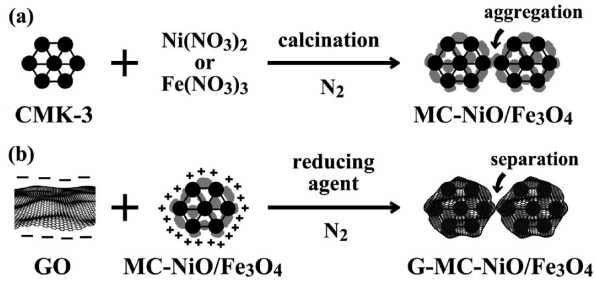

introduced into the pores of CMK-3 and then decomposed to corresponding metal oxide nanoparticles inside the pores of CMK-3. The N_2 adsorption/desorption isotherm of CMK-3 showed a type IV curve with a H1 hysteresis loop, whereas the H1 hysteresis loop in the isotherm of MC-Fe_3O_4 was not prominent (Figure S1A). Furthermore, the pore size distribution (PSD) of CMK-3 showed only one peak at 3.6 nm, corresponding to the uniform mesopore diameter, whereas the PSD of MC-Fe_3O_4 consisted of several peaks, one at 3.6 nm and others around this peak (Figure S1B), deducing that the nanoparticles had been formed in the pores, some pore channels were distorted, and some irregular pores occurred. The large pore (∼14.3 nm) existing in MC-Fe_3O_4 might result from the aggregation of large Fe_3O_4 particles formed on the surface of CMK-3. Afterward, the surface of graphene oxide (GO) was negatively charged in weak alkaline solution (pH = ∼8.0), while the surface of MC-Fe_3O_4/NiO was positively charged in weak acid solution (pH = ∼5.5) due to the large Fe_3O_4/NiO particles on the surface of CMK-3. Figure S2 shows the zeta potentials of GO, MC-Fe_3O_4, and MC-NiO in aqueous solution at different pH values. The surfaces of GO and MC-Fe_3O_4/NiO were oppositely charged over the pH range of 4−7. Therefore, after mixing the two solutions, MC-Fe_3O_4/NiO would be wrapped by GO nanosheets like candy wrapped by candy papers. Meanwhile, GO was reduced to graphene by a reducing agent (e.g., L-ascorbic acid). The graphene shell not only can protect the MC-metal oxides against disintegration and aggregation, but also improves the conductivity of the electrode and thereby enhances electron transport rate.

The contents of Fe_3O_4 and NiO in the composites were estimated by TGA. Figure S3A shows the TGA curves of MC-Fe_3O_4 and G-MC-Fe_3O_4. Since Fe_3O_4 was oxidized to Fe_2O_3 and carbon was oxidized to CO_2 after calcinations at 800 °C,[7] the Fe_3O_4 contents were calculated to be ∼62.4 wt % for MC-Fe_3O_4 and ∼50.2 wt % for G-MC-Fe_3O_4. According to the TGA curves of MC-NiO and G-MC-NiO (Figure S3B), the NiO contents were ∼62.9 wt % for MC-NiO and ∼51.8 wt % for G-MC-NiO. The morphology and structure of MC-Fe_3O_4 and G-MC-Fe_3O_4 were characterized by scanning electron microscopy (SEM) and transmission electron microscopy (TEM). Figure 1A and B shows the representative SEM images of MC-Fe_3O_4 and G-MC-Fe_3O_4, which revealed the aggregates of rodlike particles (CMK-3) with ca. 600−800 nm in length and ca. 200 nm in diameter. Moreover, some large particles with diameters of 25−35 nm could be observed on the surface of CMK-3 particles (Figure 1A). The energy dispersive X-ray spectroscopy (EDX) mapping images of Fe, O, and C elements are shown in Figure S4. The distribution of Fe and O elements was consistent with that of C, suggesting that the Fe_3O_4 particles distributed uniformly inside and outside the

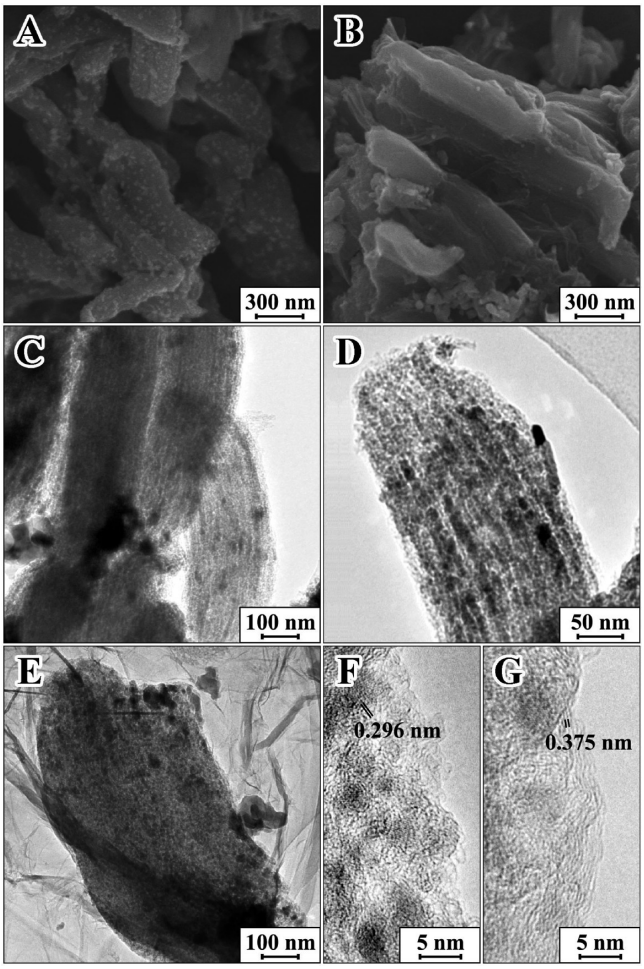

Figure 1. SEM images of (A) MC-Fe_3O_4 and (B) G-MC-Fe_3O_4. TEM images of (C, D) MC-Fe_3O_4 and (E) G-MC-Fe_3O_4. HRTEM images of (F) MC-Fe_3O_4 and (G) G-MC-Fe_3O_4.

pores of CMK-3. On the contrary, the surface of CMK-3 particles (Figure 1B) seemed pretty smooth after encapsulation, and no discernible Fe_3O_4 particles were found. Moreover, the large Fe_3O_4 particles on the surface of CMK-3 were also distinguished below the graphene by SEM (Figure S5A), suggesting that MC-Fe_3O_4 particles were completely wrapped by graphene nanosheets. Figure 1C and D shows the TEM images of MC-Fe_3O_4 at different magnifications. The as-synthesized CMK-3 was an inverse replica of SBA-15; that is, a well-ordered hexagonal array of carbon nanorods connected by some small bridges, and some large particles were present on the surface of CMK-3 (Figure 1C). On the other hand, some small particles were uniformly dispersed inside the CMK-3 framework, resulting in partial pore distortion and collapse (Figure 1D). Accordingly, the mesostructure of CMK-3 might be destroyed gradually with the increase of the metal oxide content (~62.4 wt %), and the similar phenomenon had been reported previously.[16] After encapsulation, the core−shell structure of G-MC-Fe_3O_4 was confirmed by TEM image (Figure 1E). The transparent and wrinkled graphene nanosheets were distinctly observed and tightly wrapped the MC-Fe_3O_4 particles. The edges of MC-Fe_3O_4 and G-MC-Fe_3O_4 were further observed by high-resolution TEM (HRTEM; Figure 1F and G). The size of nanoparticles (~3 nm) was definitely limited by the pore size of CMK-3 (~3.6 nm). Moreover, these nanoparticles were separated by the carbon walls of CMK-3 (Figure 1F), and the aggregation was avoided. The distance of crystal lattice fringes in the nanoparticle was ~0.296 nm, which could be assigned to the *d*-spacing of (220) plane of Fe_3O_4 crystal. After encapsulation, 2−4 layer graphene nanosheets with a lattice spacing of ~0.375 nm could be observed at the edge of G-MC-Fe_3O_4 (Figure 1G).

Subsequently, the crystalline phases of GO, MC-Fe_3O_4 and G-MC-Fe_3O_4 were identified by XRD, and their XRD patterns are shown in Figure 2A. Only one XRD peak for GO was observed at ~11°, which corresponded to a basal spacing of stacked graphene oxides (~0.8 nm). This peak disappeared in the XRD pattern of G-MC-Fe_3O_4, implying that the GO in the composite was almost reduced to the graphene. In the XRD patterns of MC-Fe_3O_4 and G-MC-Fe_3O_4, all characteristic peaks could be indexed to the cubic Fe_3O_4 structure with a = 0.8391 nm ($Fd\bar{3}m$), and no other impurity peaks were detected. As calculated by the Debye−Scherrer formula, the average crystalline size of Fe_3O_4 nanoparticles was ~32.9 nm for MC-Fe_3O_4 and 31.9 nm for G-MC-Fe_3O_4, mainly contributed by the large particles on the surface of CMK-3. Figure 2B shows the Fourier tranform infrared (FT-IR) spectra of GO, MC-Fe_3O_4 and G-MC-Fe_3O_4. Five peaks in the range of 1000−1800 cm^{-1} were observed in the FT-IR spectrum of GO, corresponding to the stretching vibrations of C═O, O−H, C−OH, C−O bonds and the skeletal vibration of C═C bond, respectively.[27] It was interesting to note that the bands corresponding to C═O, O—H, C—OH, and C═C groups were also observed in the FT-IR spectrum of modified CMK-3 (Figure S5B), whereas only O—H, C—OH, and C═C groups remained in MC-Fe_3O_4. In order to improve the adhesion of CMK-3 with metal oxide precursors, the functional groups such as carboxyl and hydroxyl were usually introduced on the walls of CMK-3 by oxidation treatment.[28] However, accompanied by the formation of Fe_3O_4 in the pores of CMK-3, the COOH group might be reduced during the thermal process. Similarly, the C═O and C—O bands were also absent in the FT-IR spectrum of G-MC-Fe_3O_4, indicating that the oxygen functional groups of GO were almost removed. The absorption band (~570.8 cm^{-1}) corresponding to the vibration of Fe−O illustrated the formation of Fe_3O_4 in MC-Fe_3O_4 and G-MC-Fe_3O_4.[29] Figure 2C shows a survey XPS spectrum of G-MC-Fe_3O_4, and the C 1s, O 1s, and Fe 2p peaks were clearly observed. Moreover, the Fe 2p XPS spectrum of G-MC-Fe_3O_4 (the inset of Figure 2C) shows two peaks located at 711.3 and 724.8 eV, corresponding to Fe $2p_{3/2}$ and Fe $2p_{1/2}$ double peaks. Note that the double peaks were broadened by virtue of the appearance of Fe^{2+} ($2p_{3/2}$ and $2p_{1/2}$), implying that the product was Fe_3O_4 rather than γ-Fe_2O_3.[29] The C 1s XPS spectra of GO and G-MC-Fe_3O_4 are shown in Figure 2D. The C 1s peak consisted of four peaks at 284.6, 286.6, 287.6, and 288.9 eV, corresponding to C—C, C—O, C═O, and O—C═O groups, respectively.[30] Compared to these peaks in the spectrum of GO, the peaks related to the oxidized groups were much weaker in the spectrum of G-MC-Fe_3O_4, also suggesting that the GO in G-MC-Fe_3O_4 was reduced by L-ascorbic acid. Moreover, the pure GO without porous carbon and Fe_3O_4 was also reduced by L-ascorbic acid under the same condition, and the product (denoted as G) was characterized using CHN analyzer. The contents of C, H and O are listed in Table S1. The C/O molar ratio of G was much higher than that of GO, confirming the high reduction degree of GO.

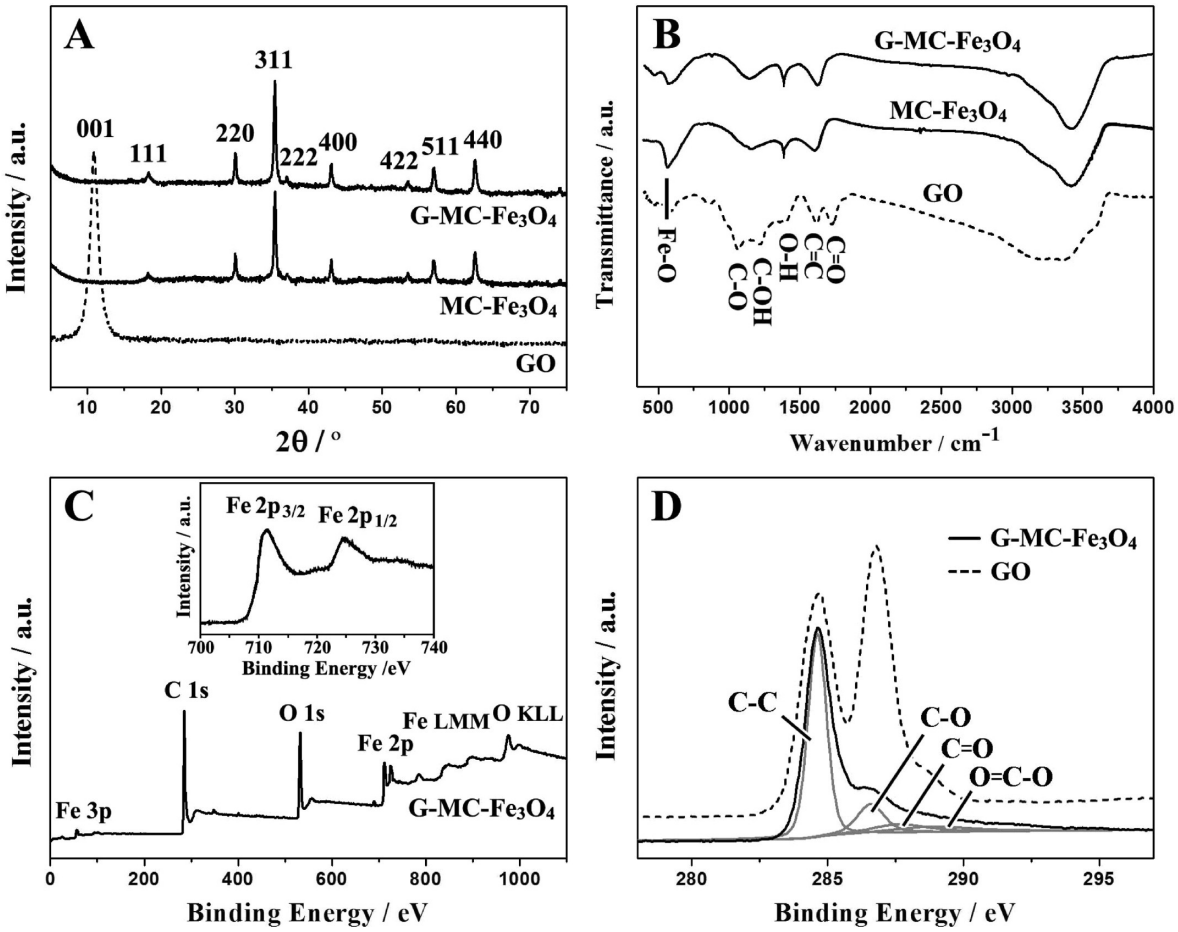

Figure 2. (A) XRD patterns and (B) FT-IR spectra of GO, MC-Fe_3O_4, and G-MC-Fe_3O_4. (C) Survey and (D) C 1s XPS spectra of G-MC-Fe_3O_4. The inset of (C) is Fe 2p XPS spectrum of G-MC-Fe_3O_4.

To identify the electrochemical reactions during cycles, cyclic voltammograms (CV) of bulk Fe_3O_4 (B−Fe_3O_4), MC-Fe_3O_4 and G-MC-Fe_3O_4 electrodes were characterized in the range of 0.01−3.0 V. Figure S6A shows the CV profiles of B−Fe_3O_4 in the first, second, third, and fifth scanning cycles. In the first cathodic scan, two reduction peaks were observed at about 1.3 and 0.2 V, corresponding to the reduction of Fe_3O_4 to Fe and the formation of a solid electrolyte interface (SEI) layer on the surface of Fe_3O_4.[7] In the first anodic scan, a broad peak was recorded at about 2.1 V, indicating the corresponding reversible reaction. In the subsequent cycles, both cathodic and anodic peaks were shifted due to the polarization of the electrode. The CV curves of MC-Fe_3O_4 (Figure S6B) were similar to those of G-MC-Fe_3O_4 (Figure S6C), which showed a cathodic peak at about 0.4 V and an anodic peak at about 1.7 V in the first cycle. Moreover, the CV curves of subsequent cycles almost overlapped, revealing a good reversibility. The electrochemical performances of B−Fe_3O_4, MC-Fe_3O_4 and G-MC-Fe_3O_4 were evaluated by galvanostatic measurements. Moreover, to deeply investigate the performance of G-MC-Fe_3O_4, graphene-encapsulated CMK-3 without Fe_3O_4 (G-MC) was also prepared. The first cycle charge−discharge curves of B−Fe_3O_4, MC-Fe_3O_4, and G-MC-Fe_3O_4 at 0.1 C (1 C = 924 mA g^{-1}) is shown in Figure 3A. A flat plateau around ∼0.8 V was present in the discharge curve, which is consistent with the previously reports for Fe_3O_4-based electrodes.[6,7] The charge and discharge capacities of G-MC-Fe_3O_4 were ca. 845 and 1333 mA h g^{-1}, higher than those of MC-Fe_3O_4 (ca. 816 and 1233 mA h g^{-1}) and B-Fe_3O_4 (ca. 757 and 1097 mA h g^{-1}). Additionally, the first discharge capacities of these samples were also higher than the theoretical capacity of Fe_3O_4, which can be ascribed to the SEI formation.[19] Figure 3B shows the cycle performances of these samples at 0.1 C. The capacity of B-Fe_3O_4 decreased rapidly to ∼100 mA h g^{-1} after 35 cycles, whereas MC-Fe_3O_4 showed good cycling stability and high stable reversible capacity at initial cycles, for example, ∼710 mA h g^{-1} after 20 cycles, due to the pores of CMK-3 that may accommodate the volume variation of Fe_3O_4 particles. Subsequently, the capacity of MC-Fe_3O_4 decreased sharply to ∼260 mA h g^{-1} after 100 cycles. The decrease in capacity of MC-Fe_3O_4 may be attributed to the gradual destruction of the mesostructure of CMK-3 during lithiation and delithiation processes, which led to partial Fe_3O_4 particles buried in carbon matrix. The large Fe_3O_4 particles on the surface of CMK-3 may also result in the capacity fading due to the loss of electronic contact after a certain time of cycling. Compared to MC-Fe_3O_4, G-MC-Fe_3O_4 exhibited better cycle stability and higher reversible capacity, for example, ∼660 mA h g^{-1} after 100 cycles. Figure 3C shows the cycle performance of G-MC prepared under the same condition but without Fe_3O_4. The capacity of G-MC after 100 cycles was ∼430 mA h g^{-1}, much smaller than that of G-MC-Fe_3O_4. Thus, according to the weight content of Fe_3O_4 (∼50.2 wt %) in G-MC-Fe_3O_4, the capacity contributed by Fe_3O_4 particles was ∼890 mA h g^{-1}, which was comparable to the theoretical capacity of Fe_3O_4. Figure 3D shows the rate capabilities of these samples at the

dx.doi.org/10.1021/am501551h | ACS Appl. Mater. Interfaces 2014, 6, 6332−6339

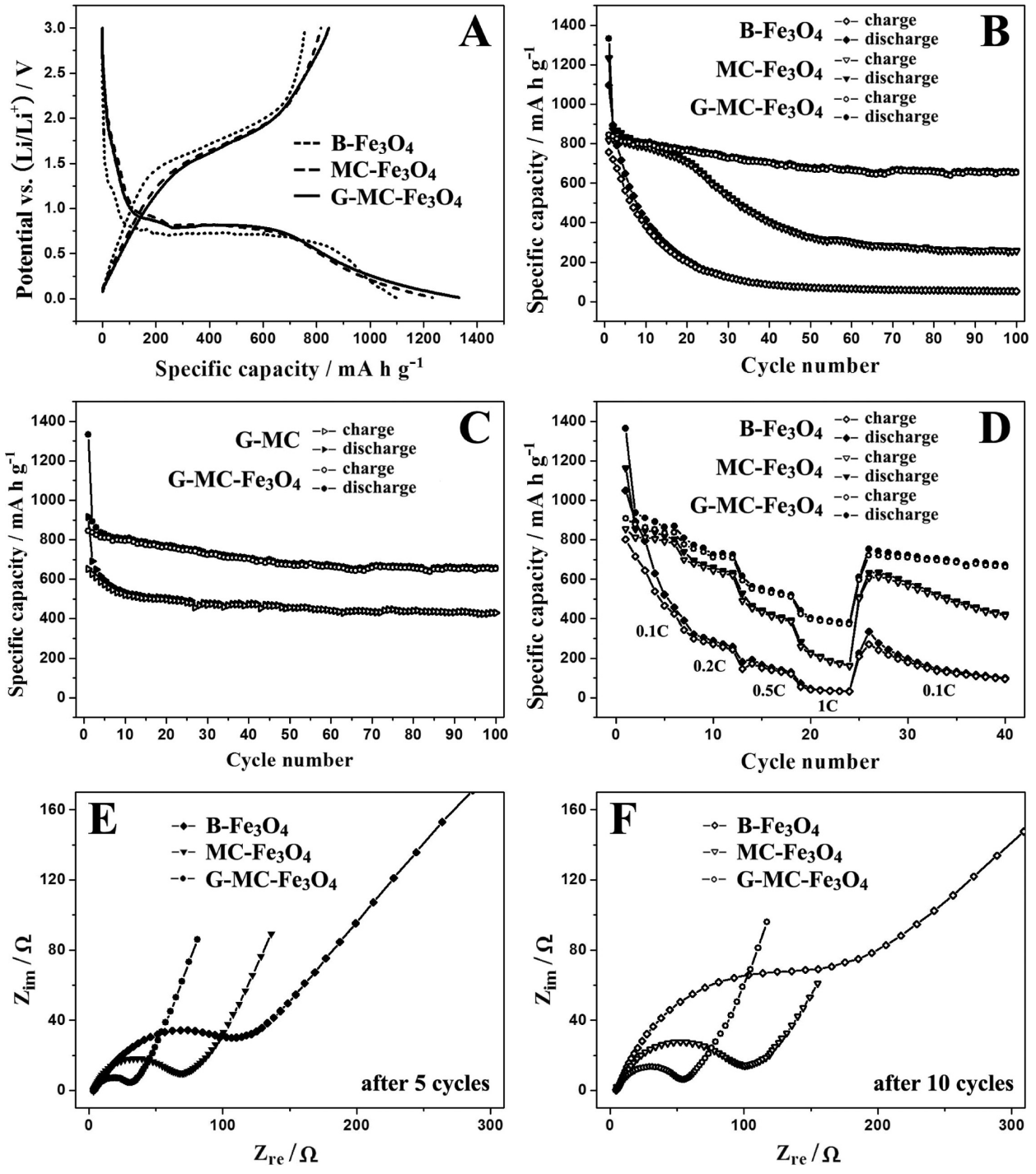

Figure 3. (A) Charge−discharge curves of B-Fe_3O_4, MC-Fe_3O_4, and G-MC-Fe_3O_4 at 0.1 C for the first cycle. (B, C) Cycle performances of these samples and G-MC at 0.1 C. (D) Rate capabilities of these samples at 0.1−1 C. (E, F) Electrochemical impedance spectra of these samples after 5 and 10 cycles.

current rates from 0.1 to 1 C. Although the capacity still decreased when the current density was increased, G-MC-Fe_3O_4 exhibited the highest capacity among these three samples. For instance, the rate capacity of G-MC-Fe_3O_4 at 1 C was ~380 mA h g^{-1}, 2.2-fold higher than that of MC-Fe_3O_4 (~170 mA h g^{-1}) and 9.5-fold higher than that of B-Fe_3O_4 (~40 mA h g^{-1}). Furthermore, a high rate capacity up to ~670 mA h g^{-1} was achieved when the current density recovered to 0.1 C, revealing its good cycling stability. The superior performance in terms of capacity and cyclability of G-MC-Fe_3O_4 may be ascribed to the graphene encapsulation, which may protect the large Fe_3O_4 particles on the surface of CMK-3, enhance the electronic conductivity of the overall electrode and possibly stabilize the mesostructure of CMK-3 during cycles. The morphology and structure of MC-Fe_3O_4 and G-MC-Fe_3O_4 after 30 cycles were characterized by SEM and TEM. Apparently, the mesostructure of CMK-3 was unstable during cycles, and large agglomerates were demonstrated in the SEM and TEM image of MC-Fe_3O_4 (Figure S7A and C). On the contrary, in the SEM and TEM images of some G-MC-Fe_3O_4

dx.doi.org/10.1021/am501551h | ACS Appl. Mater. Interfaces 2014, 6, 6332−6339

particles (Figure S7B and D), the rodlike morphology and mesostructure of CMK-3 could be observed, suggesting that the graphene may stabilize the mesostructure to some extent during cycles. To deeply investigate the improved performance of G-MC-Fe_3O_4, the EIS measurements of these samples were also carried out, and the equivalent circuit model was shown in Figure S6D. The Nyquist plots of these samples (Figure 3E and F) showed two overlapped semicircles in the high-medium-frequency region, corresponding to the Li^+ ions transport through the SEI layer (R_f) and the charge-transfer impedance (R_{ct}) on the electrode/electrolyte interface, and a sloping straight line in the low-frequency region, corresponding to the diffusion of Li^+ ions in the bulk electrode materials (Z_w). Apparently, the diameter of the overlapped semicircles for B-Fe_3O_4 was much larger than that for MC-Fe_3O_4 or G-MC-Fe_3O_4, demonstrating that graphene and CMK-3 can increase the electronic conductivity of the composite electrode. The R_{ct} value of G-MC-Fe_3O_4 after 5 cycles was ~16.2 Ω, smaller than that of MC-Fe_3O_4 (~44.2 Ω) and B-Fe_3O_4 (~73.6 Ω). Moreover, the R_{ct} value of G-MC-Fe_3O_4 slightly increased to ~32.9 Ω after 10 cycles, while the R_{ct} values of MC-Fe_3O_4 and B-Fe_3O_4 increased to ~67.4 and ~110.9 Ω, respectively. That is to say, the graphene-porous carbon-Fe_3O_4 composite possessed lowest contact and charge-transfer impedances, leading to fast electron transport during lithiation and delithiation processes and thereby resulting in significant improvement on the rate performance.

Our protocol can be further extended to the construction of graphene-encapsulated composites consisting of porous carbon and other metal oxides. For instance, MC-NiO was also prepared and wrapped by graphene nanosheets to improve its electrochemical performance. The SEM and TEM images of MC-NiO (Figure 4A and 4C) revealed that NiO nanoparticles were formed inside and outside the pores of CMK-3, which was also verified by the EDX mapping of Ni, O and C elements (Figure S8), and the rodlike MC-NiO particles randomly aggregated together. Figure 4B and D shows the SEM and TEM images of G-MC-NiO. Although some aggregates were still inevitable, these MC-NiO particles were effectively protected and separated by graphene nanosheets. The MC-NiO graphene core−shell structure could be easily observed, indicating that MC-NiO particles were well-wrapped by graphene nanosheets. Figure S9A and B shows the XRD patterns and FT-IR spectra of GO and G-MC-NiO, respectively. The XRD peaks of G-MC-NiO were indexed to the cubic NiO structure with a = 0.4195 nm ($Fm\bar{3}m$,), and the characteristic peak of GO was not detected. Moreover, only C═C, O—H, C—OH, and Ni—O bands at ca. 1593, 1383, 1228, and 420 cm^{-1} appeared in the FT-IR spectrum of G-MC-NiO, implying the reduction of GO and the presence of NiO in the composite.[2] The G-MC-NiO sample was further characterized by XPS, and the C 1s, O 1s, Ni 2p, and Ni 3p peaks were detected in the survey XPS spectrum of G-MC-NiO (Figure S9C). The fine spectrum of Ni 2p (inset of Figure S9C) exhibited two peaks at 856.0 and 873.1 eV, corresponding to $2p_{3/2}$ and $2p_{1/2}$ doublet peaks, and their satellites at 861.3 and 879.4 eV.[2] The peak in the fine spectrum of C 1s (Figure S9D) included a strong C−C peak and weak C−O, C═O, O−C═O peaks, demonstrating that the oxygen-containing groups of GO were almost removed.

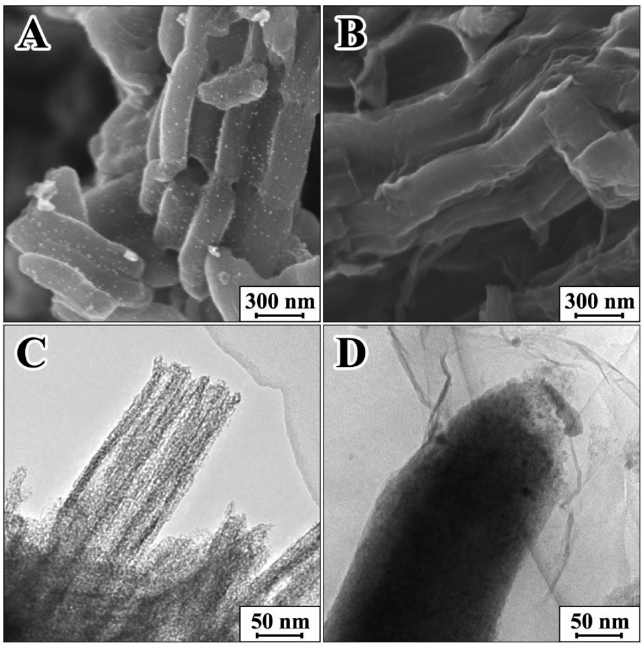

Figure 4. SEM and TEM images of (A, C) MC-NiO and (B, D) G-MC-NiO.

The electrochemical properties of MC-NiO and G-MC-NiO were also tested by CV and galvanostatic charge−discharge. Figure S10 shows the first five CV curves of MC-NiO and G-MC-NiO. There were two cathodic peaks at around 0.4 and 0.9 V in the first cycle, which were related to the first electrochemical process of NiO, including the reduction of NiO to Ni and the formation of the SEI film.[31] Two anodic peaks appeared at around 1.4 and 2.2 V, which were assigned to the regeneration of NiO and the dissolution of the SEI layer. The first cycle charge−discharge curves of these samples at 0.1 C (1 C = 718 mA g^{-1}) are shown in Figure 5A, and the flat plateau around ~0.6 V corresponded to the transformation of NiO + Li^+ to Ni + Li_2O.[2,19] Figure 5B and C shows the cycle performances and rate capabilities of these samples at 0.1 C. Apparently, G-MC-NiO showed better cycle performance and rate capability than MC-NiO. Despite a higher weight content of NiO for MC-NiO (62.9 wt %), its discharge capacity decreased remarkably to ~230 mA h g^{-1} after 100 cycles, whereas the discharge capacity of G-MC-NiO containing 51.8 wt % NiO was ~570 mA h g^{-1} after 100 cycles, higher than the theoretical capacity of the graphite electrode (372 mA h g^{-1}). Besides, a high rate capacity up to ~310 mA h g^{-1} was achieved at 1 C for G-MC-NiO, while the capacity of MC-NiO decreased obviously at each rate and was only ~130 mA h g^{-1} at 1 C. The graphene encapsulation should be conducive to the improvement of the electrochemical performance of G-MC-NiO. Figure 5D shows the electrochemical impedance spectra of these samples in the form of a Nyquist plot. The R_{ct} value of G-MC-NiO after 5 cycles was ~18.1 Ω, much lower than that of MC-NiO (~36.3 Ω), indicating that the introduction of graphene may further enhance the electronic conductivity of the electrode. This outcome validated that the electrochemical properties of porous carbon-supported metal oxides can be highly improved by graphene encapsulation.

The superior electrochemical behavior of graphene-encapsulated porous carbon−metal oxides can be assigned to the unique hierarchical structure: (i) Metal oxide particles were located inside the pores of porous carbon, which may limit the growth of metal oxides, avoid the particle aggregation and

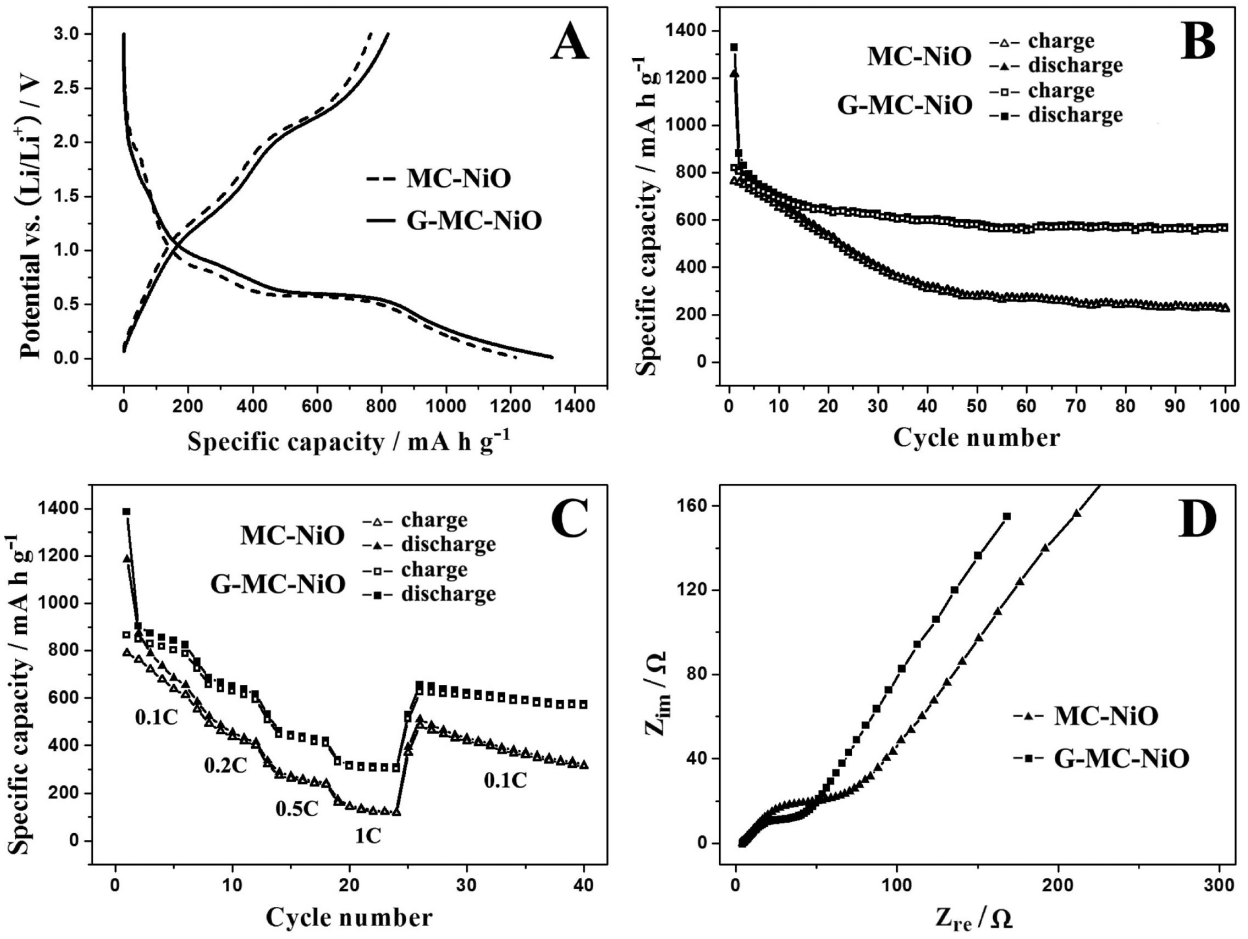

Figure 5. (A) Charge−discharge curves of MC-NiO and G-MC-NiO at 0.1 C for the first cycle. (B) Cycle performances of these samples at 0.1 C. (C) Rate capabilities of these samples at 0.1−1 C. (D) Electrochemical impedance spectra of these samples after 5 cycles.

provide free space to accommodate the volume expansion of metal oxides. (ii) The graphene encapsulation may protect the particles on the surface of porous carbon against disintegration, separate the porous carbon−metal oxide composites, and possibly stabilize the mesostructure of porous carbon during cycles. (iii) Porous carbon and graphene nanosheets may improve the electronic conductivity of the electrode and thereby enhance electron transport rate. All the above factors contributed to the high reversible capacity, good cycle performance, and good rate capability of the composites in LIBs.

CONCLUSIONS

We described a novel strategy for the preparation of graphene-encapsulated CMK-3-metal oxides by a stepwise heterocoagulation method. These advanced composites exhibited higher reversible capacities and better cycle/rate performances compared to uncoated CMK-3-metal oxides. The superior electrochemical performance can be attributed to the mesostructure of CMK-3, the graphene encapsulation and the synergetic effect between graphene and CMK-3-metal oxides. Namely, the CMK-3 and graphene nanosheets may protect and separate metal oxide particles, accommodate or restrain the volume expansion of metal oxides during cycling, and improve the electronic conductivity of the overall electrode. In addition, the graphene encapsulation may possibly tackle the collapse of the mesostructure of CMK-3 during cycles. This encapsulation approach may be developed for the fabrication of other graphene-porous carbon−metal oxide composites applied in the fields of energy conversion and storage.

ASSOCIATED CONTENT

Supporting Information

N_2 adsorption/desorption isotherms and pore size distribution of CMK-3 and MC-Fe_3O_4. FT-IR spectra of CMK-3. XRD patterns, FT-IR spectra, and XPS spectra of G-MC-NiO. Equivalent circuit for the electrochemical cells. This material is available free of charge via the Internet at http://pubs.acs.org.

AUTHOR INFORMATION

Corresponding Authors

*Tel: 86-10-58894229. Fax: 86-10-58892075. E-mail: wbyue@bnu.edu.cn (W.Y.).

*E-mail: renyu@nicenergy.com (Y.R.).

Notes

The authors declare no competing financial interest.

ACKNOWLEDGMENTS

This work was financially supported by National Natural Science Foundation of China (21101014 and 21273022).

REFERENCES

(1) Zhang, F.; Zhang, T. F.; Yang, X.; Zhang, L.; Leng, K.; Huang, Y.; Chen, Y. S. A High-Performance Supercapacitor-Battery Hybrid

Energy Storage Device Based on Graphene-Enhanced Electrode Materials with Ultrahigh Energy Density. *Energy Environ. Sci.* **2013**, *6*, 1623−1632.
(2) Yue, W. B.; Jiang, S. H.; Huang, W. J.; Gao, Z. Q.; Li, J.; Ren, Y.; Zhao, X. H.; Yang, X. J. Sandwich-Structural Graphene-Based Metal Oxides as Anode Materials for Lithium-Ion Batteries. *J. Mater. Chem. A* **2013**, *1*, 6928−6933.
(3) Lee, S.; Cho, Y.; Song, H.-K.; Lee, K. T.; Cho, J. Carbon-Coated Single-Crystal $LiMn_2O_4$ Nanoparticle Clusters as Cathode Material for High-Energy and High-Power Lithium-Ion Batteries. *Angew. Chem., Int. Ed.* **2012**, *51*, 8748−8752.
(4) Yang, S. J.; Nam, S.; Kim, T.; Im, J. H.; Jung, H.; Kang, J. H.; Wi, S.; Park, B.; Park, C. R. Preparation and Exceptional Lithium Anodic Performance of Porous Carbon-Coated ZnO Quantum Dots Derived from a Metal−Organic Framework. *J. Am. Chem. Soc.* **2013**, *135*, 7394−7397.
(5) Ming, J.; Park, J.-B.; Sun, Y.-K. Encapsulation of Metal Oxide Nanocrystals into Porous Carbon with Ultrahigh Performances in Lithium-Ion Battery. *ACS Appl. Mater. Interfaces* **2013**, *5*, 2133−2136.
(6) Chen, Y.; Xia, H.; Lu, L.; Xue, J. M. Synthesis of Porous Hollow Fe_3O_4 Beads and Their Applications in Lithium Ion Batteries. *J. Mater. Chem.* **2012**, *22*, 5006−5012.
(7) He, C. N.; Wu, S.; Zhao, N. Q.; Shi, C. S.; Liu, E. Z.; Li, J. J. Carbon-Encapsulated Fe_3O_4 Nanoparticles as a High-Rate Lithium Ion Battery Anode Material. *ACS Nano* **2013**, *7*, 4459−4469.
(8) Li, Tao.; Wang, Y. Y.; Tang, R.; Qi, Y. X.; Lun, N.; Bai, Y. J.; Fan, R. H. Carbon-Coated Fe−Mn−O Composites as Promising Anode Materials for Lithium-Ion Batteries. *ACS Appl. Mater. Interfaces* **2013**, *5*, 9470−9477.
(9) Shen, L. F.; Zhang, X. G.; Uchaker, E.; Yuan, C. Z.; Cao, G. H. $Li_4Ti_5O_{12}$ Nanoparticles Embedded in a Mesoporous Carbon Matrix as a Superior Anode Material for High Rate Lithium Ion Batteries. *Adv. Energy Mater.* **2012**, *2*, 691−698.
(10) Shen, L. F.; Uchaker, E.; Yuan, C. Z.; Nie, P.; Zhang, M.; Zhang, X. G.; Cao, G. Z. Three-Dimensional Coherent Titania−Mesoporous Carbon Nanocomposite and Its Lithium-Ion Storage Properties. *ACS Appl. Mater. Interfaces* **2012**, *4*, 2985−2992.
(11) Jung, H.; Shin, J.; Chae, C.; Lee, J. K.; Kim, J. FeF_3/Ordered Mesoporous Carbon (OMC) Nanocomposites for Lithium Ion Batteries with Enhanced Electrochemical Performance. *J. Phys. Chem. C* **2013**, *117*, 14939−14946.
(12) Yu, H. J.; Zhao, Y. F.; Zhou, C.; Shang, L.; Peng, Y.; Cao, Y. H.; Wu, L.-Z.; Tung, C.-H.; Zhang, T. R. Carbon Quantum dots/TiO_2 Composites for Efficient Photocatalytic Hydrogen Evolution. *J. Mater. Chem. A* **2014**, *2*, 3344−3351.
(13) Li, H. F.; Zhu, S. M.; Xi, H. A.; Wang, R. D. Nickel Oxide Nanocrystallites within the Wall of Ordered Mesoporous Carbon CMK-3: Synthesis and Characterization. *Microporous Mesoporous Mater.* **2006**, *89*, 196−203.
(14) Qiao, H.; Li, J.; Fu, J. P.; Kumar, D.; Wei, Q. F.; Cai, Y. B.; Huang, F. L. Sonochemical Synthesis of Ordered SnO_2/CMK-3 Nanocomposites and Their Lithium Storage Properties. *ACS Appl. Mater. Interfaces* **2011**, *3*, 3704−3708.
(15) Nagao, M.; Otani, M.; Tomita, H.; Kanzaki, S.; Yamada, A.; Kanno, R. New Three-Dimensional Electrode Structure for the Lithium Battery: Nano-Sized γ-Fe_2O_3 in a Mesoporous Carbon Matrix. *J. Power Sources* **2011**, *196*, 4741−4746.
(16) Zhang, H. J.; Tao, H. H.; Jiang, Y.; Jiao, Z.; Wu, M. H.; Zhao, B. Ordered CoO/CMK-3 Nanocomposites as the Anode Materials for Lithium-Ion Batteries. *J. Power Sources* **2010**, *195*, 2950−2955.
(17) Cheng, M.-Y.; Hwang, B.-J. Mesoporous Carbon-Encapsulated NiO Nanocomposite Negative Electrode Materials for High-Rate Li-Ion Battery. *J. Power Sources* **2010**, *195*, 4977−4983.
(18) Novoselov, K. S.; Geim, A. K.; Morozov, S. V.; Jiang, D.; Katsnelson, M. I.; Grigorieva, I. V.; Dubonos, S. V.; Firsov, A. A. Two-Dimensional Gas of Massless Dirac Fermions in Graphene. *Nature* **2005**, *438*, 197−200.
(19) Yue, W. B.; Lin, Z. Z.; Jiang, S. H.; Yang, X. J. Preparation of Graphene-Encapsulated Mesoporous Metal Oxides and Their Application as Anode Materials for Lithium-Ion Batteries. *J. Mater. Chem.* **2012**, *22*, 16318−16323.
(20) Yang, S.; Yue, W. B.; Zhu, J.; Ren, Y.; Yang, X. J. Graphene-Based Mesoporous SnO_2 with Enhanced Electrochemical Performance for Lithium-Ion Batteries. *Adv. Funct. Mater.* **2013**, *23*, 3570−3576.
(21) Yue, W. B.; Yang, S.; Ren, Y.; Yang, X. J. In Situ Growth of Sn, SnO on Graphene Nanosheets and Their Application as Anode Materials for Lithium-Ion Batteries. *Electrochim. Acta* **2013**, *92*, 412−420.
(22) Yue, W. B.; Tao, S. S.; Fu, J. M.; Gao, Z. Q.; Ren, Y. Carbon-Coated Graphene−Cr_2O_3 Composites with Enhanced Electrochemical Performances for Li-Ion Batteries. *Carbon* **2013**, *65*, 97−104.
(23) Zhou, G. M.; Wang, D.-W.; Li, F.; Zhang, L. L.; Li, N.; Wu, Z.-S.; Wen, L.; Lu, G. Q.; Cheng, H.-M. Graphene-Wrapped Fe_3O_4 Anode Material with Improved Reversible Capacity and Cyclic Stability for Lithium Ion Batteries. *Chem. Mater.* **2010**, *22*, 5306−5313.
(24) Wang, J.-Z.; Zhong, C.; Wexler, D.; Idris, N. H.; Wang, Z.-X.; Chen, L.-Q.; Liu, H.-K. Graphene-Encapsulated Fe_3O_4 Nanoparticles with 3D Laminated Structure as Superior Anode in Lithium Ion Batteries. *Chem.—Eur. J.* **2011**, *17*, 661−667.
(25) Jun, S.; Joo, S. H.; Ryoo, R.; Kruk, M.; Jaroniec, M.; Liu, Z.; Ohsuna, T.; Terasaki, O. Synthesis of New, Nanoporous Carbon with Hexagonally Ordered Mesostructure. *J. Am. Chem. Soc.* **2000**, *122*, 10712−10713.
(26) Hummers, W. S.; Offeman, R. E. Preparation of Graphitic Oxide. *J. Am. Chem. Soc.* **1958**, *80*, 1339−1339.
(27) Zhao, L.; Yue, W. B.; Ren, Y. Synthesis of Graphene-Encapsulated Mesoporous In_2O_3 with Different Particle Size for High-Performance Lithium Storage. *Electrochim. Acta* **2014**, *116*, 31−38.
(28) Zhu, S. M.; Gu, J. J.; Chen, Z. X.; Dong, J. P.; Liu, X. Y.; Chen, C. X.; Zhang, D. Controlled Synthesis of Polyaniline Inside Mesoporous Carbon for Electroanalytical Sensors. *J. Mater. Chem.* **2010**, *20*, 5123−5128.
(29) Su, J.; Cao, M. H.; Ren, L.; Hu, C. W. Fe_3O_4−Graphene Nanocomposites with Improved Lithium Storage and Magnetism Properties. *J. Phys. Chem. C* **2011**, *115*, 14469−14477.
(30) Shang, L.; Bian, T.; Zhang, B. H.; Zhang, D. H.; Wu, L.-Z.; Tung, C.-H.; Yin, Y. D.; Zhang, T. R. Graphene-Supported Ultrafine Metal Nanoparticles Encapsulated by Mesoporous Silica: Robust Catalysts for Oxidation and Reduction Reactions. *Angew. Chem.* **2014**, *126*, 254−258.
(31) Liu, H.; Wang, G. X.; Liu, J.; Qiao, S. Z.; Ahn, H. J. Highly Ordered Mesoporous NiO Anode Material for Lithium Ion Batteries with an Excellent Electrochemical Performance. *J. Mater. Chem.* **2011**, *21*, 3046−3052.